Spatiotemporal control of liquid crystal structure and dynamics through activity patterning

Rui Zhang [1,11,12], Steven A. Redford [2,3,12], Paul V. Ruijgrok [4], Nitin Kumar [3,5], Ali Mozaffari [1], Sasha Zemsky[6], Aaron R. Dinner [3,7], Vincenzo Vitelli [3,8], Zev Bryant [4,9], Margaret L. Gardel [1,3,8 ✉] and Juan J. de Pablo [1,10 ✉]

Active materials are capable of converting free energy into mechanical work to produce autonomous motion, and exhibit striking collective dynamics that biology relies on for essential functions. Controlling those dynamics and transport in synthetic systems has been particularly challenging. Here, we introduce the concept of spatially structured activity as a means of controlling and manipulating transport in active nematic liquid crystals consisting of actin filaments and light-sensitive myosin motors. Simulations and experiments are used to demonstrate that topological defects can be generated at will and then constrained to move along specified trajectories by inducing local stresses in an otherwise passive material. These results provide a foundation for the design of autonomous and reconfigurable microfluidic systems where transport is controlled by modulating activity with light.

Soft materials in which individual components convert ambient free energy into mechanical work are commonly referred to as active matter[1,2]. These systems are compelling in that their relatively simple rules of propulsion and inter-particle interactions can give rise to intriguing collective behaviours and pattern formation across length scales[3,4]. Active components underpin coherence in a wide range of natural processes. They play a critical role in cellular migration, flocking and long-range flows in dense bacterial suspensions[5–10]. These behaviours are not just interesting in and of themselves, but hold promise as the basis for the design of novel, functional materials[11,12]. The central challenge of engineering functionality in active materials is that active flows are often turbulent[13–17]. Efforts to control these flows thus far have utilized physical boundaries to constrain the material, and rely on spontaneous symmetry breaking to yield steady states and coherent dynamics over large scales[18–22]. While these works have demonstrated that a degree of control in active systems is indeed possible, the dependence on physical barriers and spontaneous symmetry breaking limits the amount of control that can be exerted. We seek a different control parameter with which we may direct the flow and dynamics of an active material without the malice of forethought. Ideally, this more flexible control parameter could direct the material asymmetrically and thus allow for the programming of more complex behaviours in active systems. In this Article, we introduce spatially dependent activity as this flexible control parameter, and demonstrate both in experiment and simulations how it can be leveraged to direct defect dynamics and control long-range flows in an active nematic liquid crystal.

High activity regions in nematics are self-contained
Nematic liquid crystals (nematics) are a phase of matter in which extended components—mesogens—align along their long axis to form a material with long-range orientational order, but which can flow like a liquid[23]. Structural disorder in these systems is stored in distinct regions of discontinuity termed topological defects[23]. In two dimensions, topological defects carry a 'charge' of either $+\frac{1}{2}$ or $-\frac{1}{2}$, defined by the winding number about the defect core (Fig. 1a). When extensile stress is introduced along the orientation of the mesogens, the asymmetric $+\frac{1}{2}$ defects are propelled along their axis of symmetry[24]. The interplay between the active and elastic stress leads to a steady-state nucleation, motion and annihilation of defects, resulting in a state known as 'active turbulence'[14,25,26]. One useful class of active liquid crystals is those formed by cytoskeletal polymers[13,27]. Activity is readily introduced to these systems via the addition of molecular motor proteins that slide adjacent filaments past each other, thereby generating extensile stresses along the nematic orientation[28]. In this work we construct a nematic liquid crystal by crowding short (~1 μm in length) actin filaments (F-actin) onto an oil–water interface[29] (Fig. 1b). Because of the fluorescent dye and the polarized laser used in these experiments, filaments that are vertical in the experimental frame appear brighter than those which are horizontal. Thus, pixel intensity tells us about the local orientation of the nematic field[30,31] (see Fig. 1a and Methods section).

While previous realizations of cytoskeletal liquid crystals have harnessed the power of naturally occurring motor proteins[13,20,27], in this work we produce spatially structured activity by exploiting motor proteins engineered with light-dependent gliding velocities[32,33]. This strategy is distinct from that employed in earlier work, where optically controlled reversible cross-linking of motors or inhibitor deactivation was used to induce stress in cytoskeletal assemblies[33–35]. The light-activated gear-shifting myosin motors used here are constructed from myosin XI catalytic heads and a lever arm containing the light-sensitive LOV2 domain. The stimulated
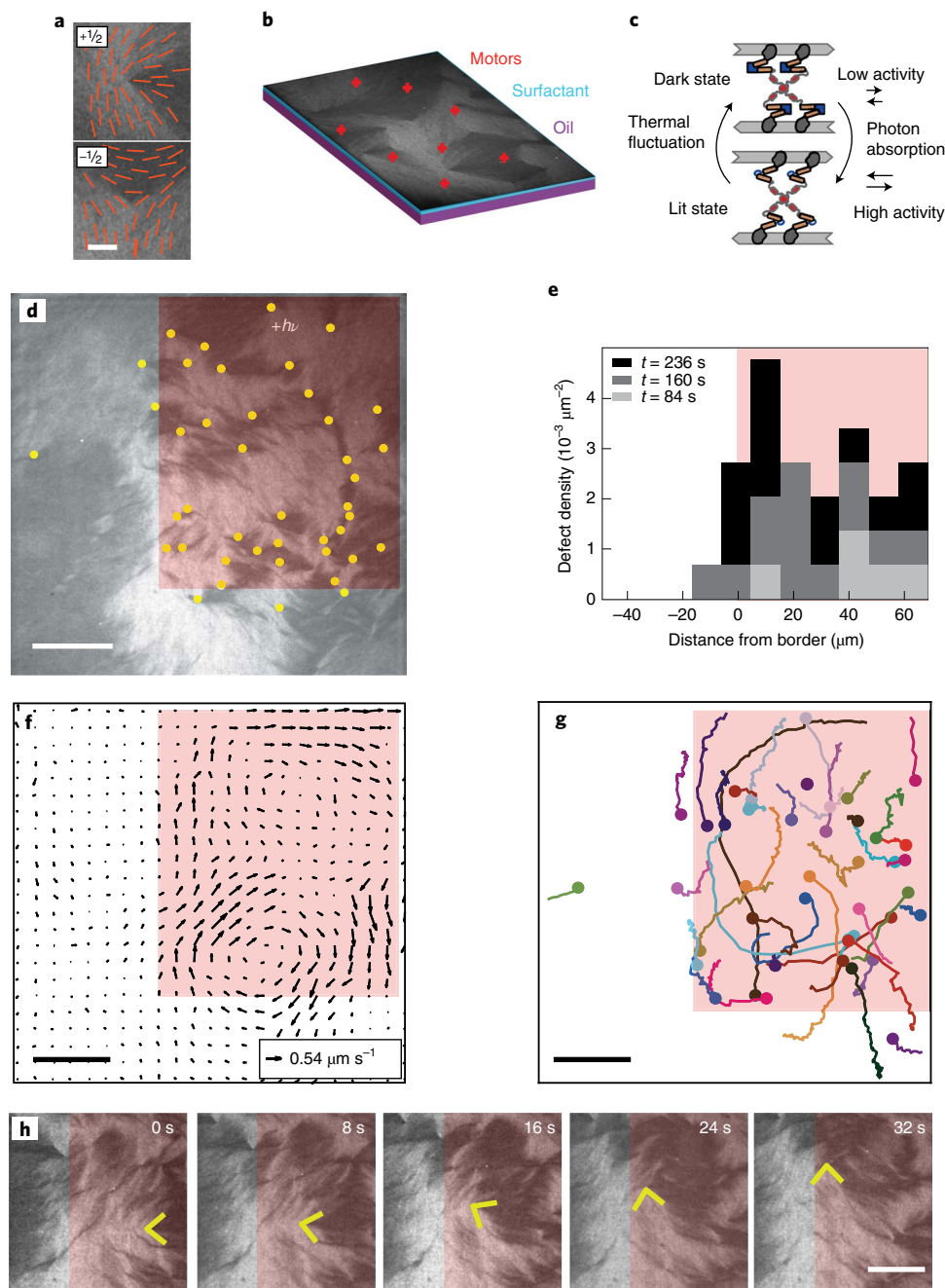
Fig. 1 | Patterning activity in an actin liquid crystal leads to spatially confined flows and topological defects. a, Polarization image of actin filaments forming a +½ (top) and −½ (bottom) defect. Brighter (darker) pixels in the image are regions in which filaments are vertical (horizontal). Red lines indicate the local average orientation of filaments (director). Scale bar, 5 μm. **b**, Schematic of the experimental setup. Actin is crowded onto an oil–water interface by methylcellulose (not pictured) where engineered myosin motors generate active stress. **c**, Schematic illustrating the gear-shifting motors. The tetrameric myosin motors are constructed with engineered lever arms that contain the light-sensitive LOV2 domain from *Avena sativa*. Top (dark state): in the absence of blue light, the LOV2 domain adopts a folded conformation (blue squares), acting as a mechanical element with some rigidity. Bottom (lit state): upon absorption of 470 nm light (downward kinetic arrow) part of the LOV2 undocks and becomes disordered, now acting as a flexible linker (blue linkages). The undocked LOV2 reverts back to the folded conformation in a thermally activated process (upward kinetic arrow), with motors re-populating the dark state. The light-dependent conformational changes of the lever arm alter the working stroke of the motors; in the context of cross-linked actin filaments we propose that this results in a higher sliding velocity in the lit state ('high activity') than in the dark state ('low activity'), corresponding to the velocity change seen in gliding filament assays[33]. **d**, Experimental polarization microscopy snapshot of fluorescently tagged actin driven by MyLOVChar4~1R~TET. Conditions are as detailed in Supplementary Table 1, 'Fig. 1'. Gear-shifting motors were stimulated only within the red box labelled '+*hν*'. Topological defects as described above are indicated by yellow dots. Scale bar 20 μm. **e**, Histogram of snapshots of the defect density along the *x*-axis over time for Supplementary Video 2 shown in **d**. Darker colours indicate later time points. **f**, Velocity field corresponding to the frame in **d**. Scale bars in **f** and **g**, 20 μm. **g**, The +½ defect trajectories for the first 400 s of stimulation for the experiment excerpted in **d**. **h**, Example of a trajectory in which a defect 'deflects' off of the boundary of the stimulated region. The defect is marked by a yellow chevron. Scale bar, 10 μm.

unfolding of this LOV2 domain changes the geometry and effective length of the lever arm, conferring optical modulation of motor velocity on the biopolymer F-actin[32]. To generate local stress on antiparallel F-actin, engineered oligomerization domains are utilized to create motor tetramers[33,36] (Fig. 1c). These tetramers, when added to actin liquid crystals, produce higher defect densities and a greater average nematic speed upon stimulation (Supplementary Fig. 1 and Supplementary Video 1). To target this increase in activity to just one region of the liquid crystal a micromirror array is used to selectively target the stimulation wavelength of 470 nm to one portion of the sample, while confocal fluorescence imaging is used to visualize fluorescently tagged actin.

We selectively illuminate a large region (~2,000 μm²) (Fig. 1d, red box) in a liquid crystal containing gear-shifting motors. Upon stimulation, the density of topological defects remains low outside of the stimulated region while the activity within leads to defect proliferation (Fig. 1d, yellow circles). This transition from low to high defect density is sharp, occurring within several micrometres of the boundary (Fig. 1e). Moreover, the nematic spontaneously flows within the illuminated region, with an instantaneous velocity that is threefold larger than that outside the bounds (Fig. 1f). While large when compared with the unstimulated region, this flow is hampered when compared with an unconstrained nematic driven by the same motors (Supplementary Fig. 2). That defect density and nematic velocity sharply decrease as one leaves the stimulated region implies a sort of confinement of activity within the stimulated region. This confinement can be visualized by tracking the location of +½ defects over time. These trajectories are largely contained within the illuminated region over 400 s, only rarely crossing over from one region to another (Fig. 1g and Supplementary Video 2). This observation holds promise for engineering applications, particularly for the control of individual defect dynamics. Consider the example in Fig. 1h: as the defect approaches the border it is deflected. That is, it undergoes a sharp reorientation such that it never crosses the boundary. This implies that a judicious choice of border geometry could allow for the design of motile defect trajectories. This key observation motivated us to explore the extent to which patterned activity could be harnessed to control the proliferation and deflection of defects in active nematics. With this, we envision the capability to arbitrarily pattern active flows and manipulate transport.

Relative activity is key for defect confinement

The above experimental observations demonstrate how the difference between the activity in the stimulated and unstimulated regions can be used to spatially confine topological defects. To further understand the extent and utility of such an effect for the precise control of defects, we turn to comprehensive hydrodynamic simulations of active liquid crystals. Our model is based on a Q-tensor representation of the nematic liquid crystal that incorporates hydrodynamic interactions[37,38]. The activity α is introduced as a local force dipole such that the active stress in an incompressible active liquid crystal[39] is $\mathbf{\Pi} = -\alpha \mathbf{Q}$. Previously, we and others have considered α to be constant[24,27,28,38,40]. We now consider α as a spatial variable, which gives rise to a new stress term due to the gradient of α. Here, a hybrid lattice Boltzmann approach is used to solve the governing equations (see the Simulation model section). This method has been shown to be successful in capturing active nematic behaviours over a range of activities[27,40], including the high activity 'active turbulent' regime in which topological defects are continuously generated, propelled and annihilated to generate chaotic-like flows[14,25,26]. While more work is needed to quantitatively relate α to the biophysical properties of actomyosin motors, our experiments show that when optogenetic myosins are switched between low-velocity and high-velocity states, the resulting characteristics of the nematic are consistent with increasing α (Supplementary Fig. 2)[27]. As such, we can rely on nemato-hydrodynamic simulations

to explore how spatial variation in activity can be used as a tool to control active matter.

We first consider a nematic comprised of two regions of differing activity, α_1 and α_2, with a flat interface at $x = 0$. For $x < 0$ the nematic has a uniform activity of magnitude α_1, and for $x > 0$ the activity is α_2. Figure 2a,b shows snapshots of the dynamic steady-state configurations of the nematic order (lines) and instantaneous velocity, respectively, for simulations with $\alpha_1 = 0.0001$ and $\alpha_2 = 0.005$. All simulation data are shown in lattice units where the unit length is chosen to be the mesogen length (see the Simulation model section). We identify an interfacial region $x_1 \leq x \leq x_2$ within which the −½ defect density deviates from that expected for an active nematic of uniform activity equivalent to α_1 and α_2; that is, for $x > x_2$ the −½ defect density equals that for a bulk nematic with activity α_2 (Fig. 2c). As in experiment, the trajectories of the +½ defects created in the $x > 0$ region rarely cross into the low activity region $x < 0$ (Fig. 2d).

To consider the transition between these two regions, we plot the spatial profile of the both +½ and −½ defects across the interface (Fig. 2c). In simulations where $\alpha_1 = 0.0001$ and $\alpha_2 = 0.005$ the density profile for −½ topological defects exhibits a pronounced peak near the interface (Supplementary Figs. 3 and 4). By contrast, the distribution function for +½ defects is flatter and extends into the less active side. The accumulation of defects at the interface gives rise to a topological-charge dipole moment, similar to a recent theoretical calculation for a dry active nematic[41], and not unlike that encountered at the interface between charged species of different dielectric permittivity[42]. As defects try to cross from a high (α_2) to a low (α_1) active region, they lose mobility and appear to experience an elastic attraction from the opposite-charge defects in the active region. This prevents them from straying deeper into the low-activity side (Supplementary Video 3). To quantify the sharpness of these defect-density distributions, we identify the transition region, $w_\rho = x_2 - x_1$, the ends of which are those points where the defect density deviates from that expected for a nematic with uniform activity (Fig. 2d). This width, w_ρ, is effectively a measure of the confinement induced by the difference in activity at the interface.

To determine how changes in relative activity impact confinement, we explore how the width of the transition region varies as a function of α_1, for simulations with fixed $\alpha_2 = 0.005$. We find that w_ρ is of the same order of magnitude, and approximately 100-fold that of the nematic coherence length (the liquid crystal's intrinsic length scale that is associated with its defect core size), for all relative activities $\alpha_1/\alpha_2 < 0.5$ (Fig. 2e). As α_1 approaches α_2, the interfacial width w_ρ increases (see Fig. 2e and Supplementary Fig. 3). Likewise, for a given set of activities, the interfacial width is also quite sensitive to the friction, increasing as the friction is decreased (Supplementary Fig. 5). Thus, both friction and relative activity can be tuned to construct a sharp interface for defect confinement. Note that friction is introduced by the viscous damping of the flow by the confining surfaces where there is a no-slip hydrodynamic boundary condition. This is equivalent to setting a length scale beyond which hydrodynamic forces are screened. One could imagine that this might correspond to the amount of fluid that an experimental sample advects due to the thickness of the sample.

In simulations, we also find that the emergence of defect confinement is accompanied by a preferential mesogen orientation perpendicular to the boundary, creating a so-called 'anchoring effect' driven by activity gradients. As seen in Fig. 2a, the directors on the low-activity side adopt a normal orientation to the interface. To characterize the anchoring near to and at the interface, we define an order parameter, $P_2(\mathbf{n} \cdot \boldsymbol{\nu}) = \langle(3(\mathbf{n} \cdot \boldsymbol{\nu})^2 - 1)\rangle / 2$, where $\mathbf{n}$ is the director field, $\boldsymbol{\nu}$ is the interfacial normal of the activity boundary, and $\langle \rangle$ denotes an ensemble average. At $x = 0$, no anchoring is observed for any relative activity levels (Fig. 2f, blue squares). However, at $x = x_1$, normal anchoring becomes prominent for relative activities
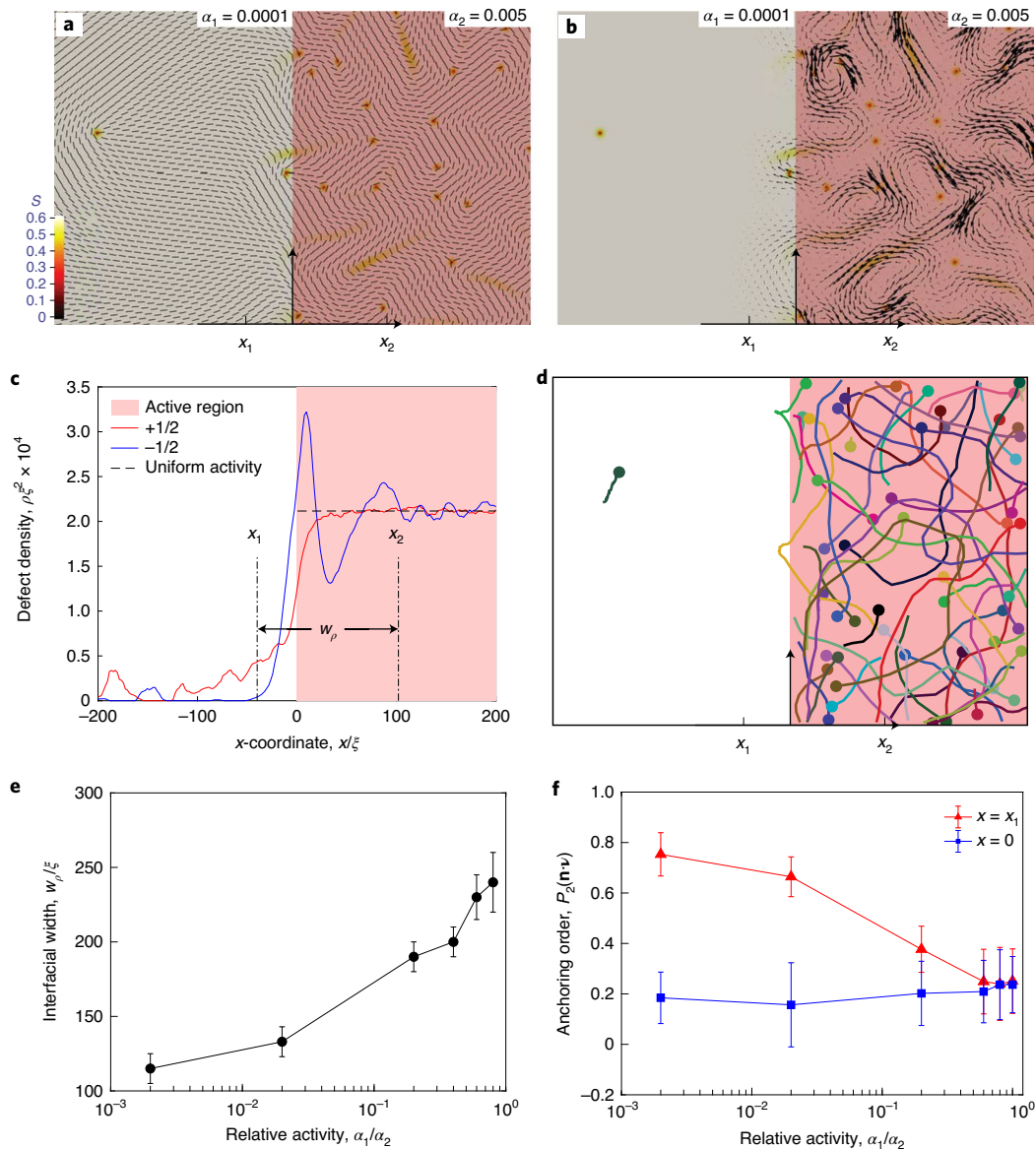
Fig. 2 | Simulations of defect behaviour in a patterned active nematic. a–d, Snapshot of the director field near the boundary between the higher and lower activity regions, located at $x=0$ (**a**), its corresponding velocity field (**b**), defect density profile (averaged over ten ensembles of duration 1,000τ) (**c**) and defect trajectories (**d**). The active region is coloured light red in **a–c**. The background in **a,b** is coloured with the nematic order parameter S, with dark red indicating defect locations. **e**, Defect density interfacial width, w_ρ, as a function of relative activity, α_1/α_2. **f**, Scalar order parameter $P_2(\mathbf{n}\cdot\mathbf{v})$ characterizing the anchoring effect at different locations with respect to the boundary of the activity pattern. The error bars in **e** and **f** represent the standard deviations over 100 ensembles.

less than 0.1 when the interface is prominent (Fig. 2f, red triangles; see also Supplementary Fig. 6). Thus, a sharp gradient in activity simultaneously constrains defects to the region of higher activity and anchors the director field in the low-activity region in the direction normal to the interface. Together, these results further suggest that structured activity is a means to control nematics regionally, at scales much larger than the defect spacing, potentially providing more flexibility than that previously demonstrated with physical barriers[20,21].

Structured stresses can yield controlled defect nucleation
We next use simulations to explore the minimum length scale at which structured activity can be used to manipulate liquid crystals. In particular, the extent to which spatially structured activity can be utilized to create and manipulate defects. In nematics with homo-

geneous activity, defect creation arises from instabilities in bending undulations[15,43]. The level of active stress sets the undulation wavelength λ and, therefore, sets a length scale required for defect nucleation[24]. We first consider the effects of adding activity ($\alpha=0.03$) within a rectangular region, with dimensions slightly larger than this natural length scale $\sqrt{K/\alpha}$, with K being the elastic constant, in an initially uniform nematic (Fig. 3a, inset). Because of the mirror or D_2 symmetry of the rectangular pattern, the resulting elastic distortions and hydrodynamic flows preserve such symmetry. Therefore, two bending undulations emerge at the two sides of the activity pattern with equal strength. Each of them gives rise to a pair of $\pm\frac{1}{2}$ defects simultaneously (Fig. 3a and Supplementary Video 4). The direction of the initial undulations can be understood by analysing the contribution of the activity gradient at the defect pattern (see Supplementary Information and Supplementary Fig. 7).
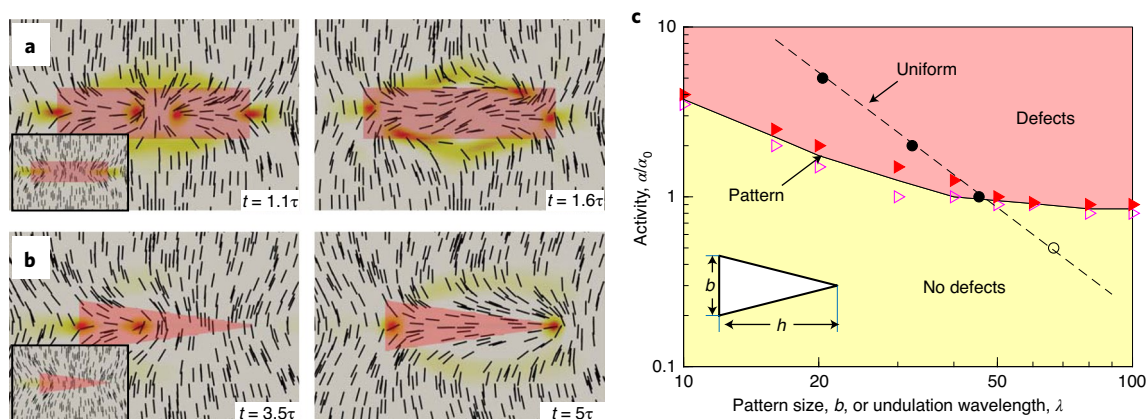
Fig. 3 | Simulations of defect-pair creation using activity pattern. a,b, Sequential images of an initially uniform active nematic with a rectangular (**a**) and a triangular (**b**) pattern at an activity level $\alpha = 3\alpha_0$. Initial configurations are shown in the insets of **a** and **b**. The triangular (rectangular) region has a base (height) $b = 14$ and a height (width) $h = 50$. **c,** Threshold activity for different pattern sizes at a fixed aspect ratio $h/b = 3$ is shown as triangle symbols. Spontaneous undulation wavelengths at a given activity are shown as circle symbols. Open symbols indicate no defect generation; filled symbols indicate defect generation.
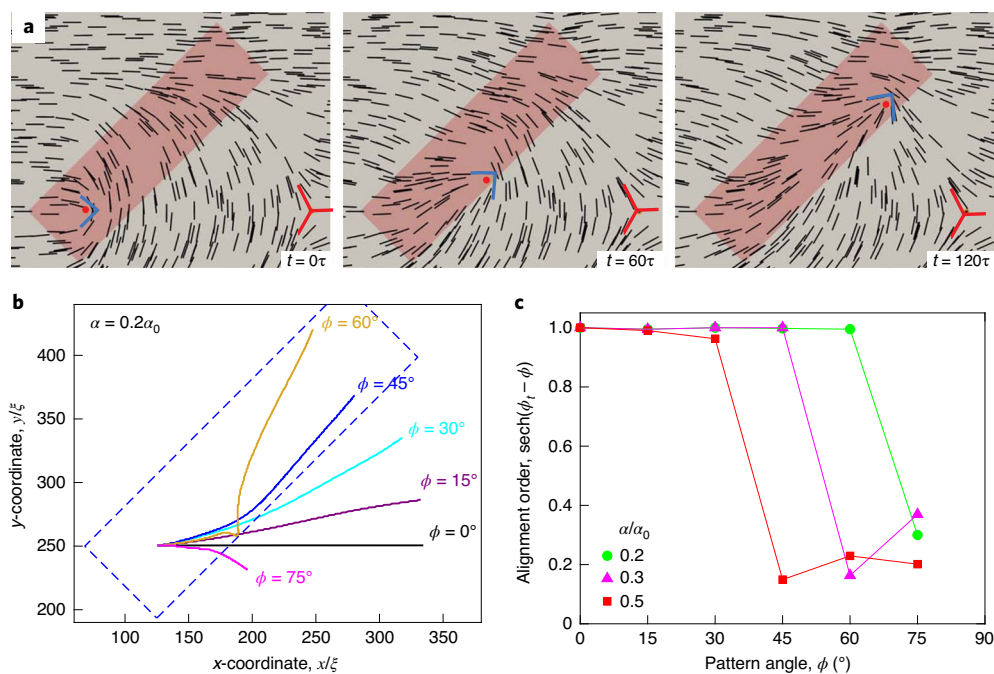

Fig. 4 | Simulations of defect deflection by a rectangular activity pattern. a, Sequential images showing defect deflection at activity $\alpha = 0.2\alpha_0$ and box tilt angle $\phi = 45°$. Initial defect separation is 250. A rectangle size (290 × 80) is chosen such that the pattern length can cover the two defects when horizontally placed, and the width is neither too narrow, so that the activity can still drive the defect, nor too wide so as to lose guidance. Defects are marked to aid the eye. **b,** Defect trajectories for different tilt angles at $\alpha = 0.2\alpha_0$. The activity pattern is shown as a dashed box for $\phi = 45°$. **c,** The aligning order parameter $\mathrm{sech}(\phi_t - \phi)$ as a function of the imposed angle ϕ for various activities where ϕ_t is the angle of the asymptotic trajectory with respect to $+x$.

Note that for an even higher activity level, more than two defect pairs can be generated using this activity pattern. While creating defects in this manner is promising, we desire asymmetric control such that we can create single pairs of defects. To break the symmetry of the rectangle, we consider a triangular region with a base b and height h of similar dimensions to the rectangle (Fig. 3b). In what follows, the length unit ξ of these dimensions is omitted for conciseness. Here, activity-induced bending instabilities incline towards the triangle tip and lead to the formation of a single pair of $\pm\frac{1}{2}$ defects. To determine how defect-pair creation depends on the triangle size and activity level, we perform simulations over a range

of activities and pattern size b, for a given aspect ratio $h/b = 3$. For a given size b, we map out the threshold activity required to generate a defect pair (Fig. 3c and Supplementary Video 5). When $b > 50$, the pattern becomes sufficiently large that it surpasses the bending undulation wavelength in a uniform nematic (Fig. 3c, dashed line). Here the threshold level of activity, α_0, required to generate a defect pair is similar to that found in a nematic with homogeneous activity and, as may be expected, more than one defect pair can be created. For $b < 50$, the activity level required to generate a defect pair increases as the required length scale decreases (Fig. 3c, red triangles). However, we find the stress needed is less than would be
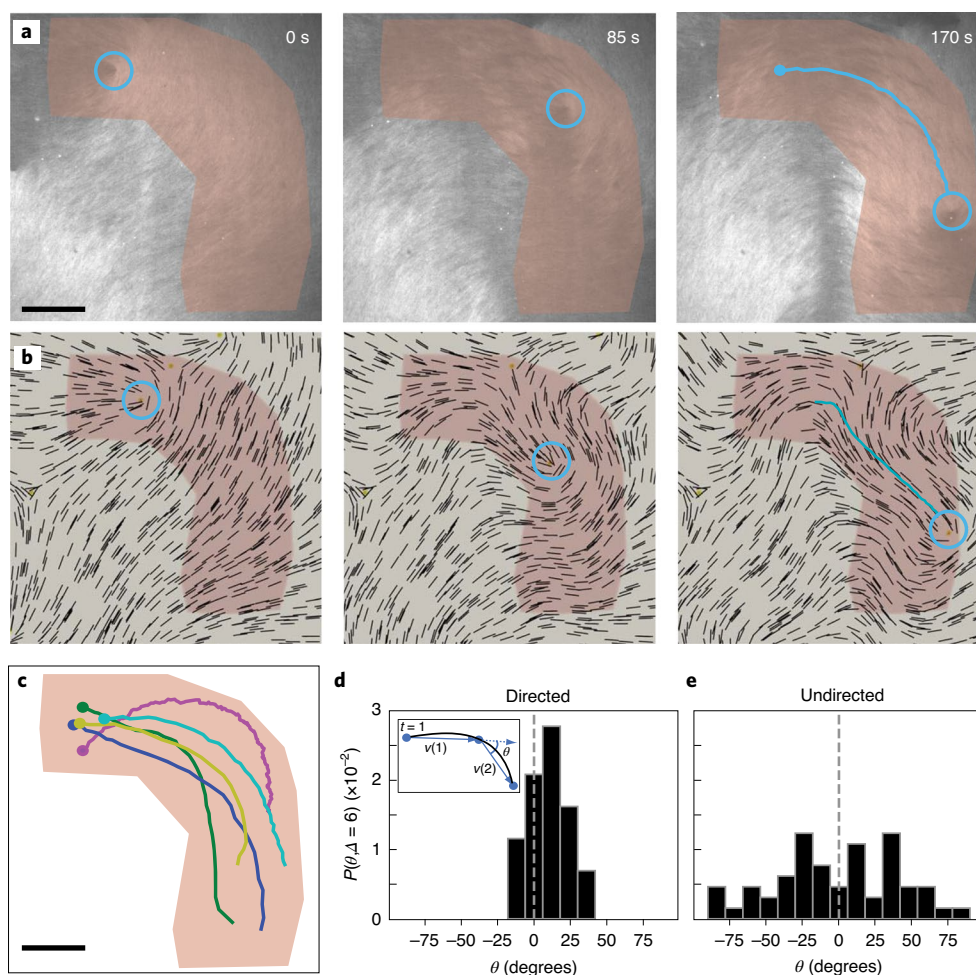
Fig. 5 | Targeted activation can be used to direct defect trajectories in experiment and simulation. a, Series of experimental images showing a +½ defect (circled in blue) moving within the active pattern (red outline). The trajectory of the defect is shown as a tail on the defect in the last frame. **b**, Series of snapshots from simulations showing the motion of a defect in an activity pattern that mimics the experiment shown in **a**. **c**, Trajectories for five independent experimental samples from two different days (scatterplot) in relation to the activated region. **d**, PDF for a given change in vector angle, θ, for the trajectories in **c**. Inset is a schematic of the method for quantifying the angle change. The grey dashed line indicates an angle of 0°. **e**, PDF of change in vector angle for Supplementary Video 1. The time lag in both **d** and **e** is 25 s, see Methods for a full treatment of the turn angle and Supplementary Fig. 6 for the turn angle at other lag times. Scale bars are 20 μm.

required for defect generation in the absence of structured activity (Fig. 3c, filled black circles). Indeed, the activity gradient creates an additional stress that contributes to defect nucleation. By changing the geometry of the pattern, the threshold activity of defect generation can be varied (Supplementary Fig. 8). Thus, a judicious choice of activity and geometry allows for control of the nematic field at the scale of individual topological defects.

Confinement affords control of defect trajectories

Having demonstrated the potential for control over defect creation, we next use simulations to consider the extent to which local activity gradients can control the movement of pre-existing defects. First, we consider a passive nematic in which a +½ defect is oriented towards a −½ defect and is separated by a distance $d = 250$, as shown in Fig. 4a. With this geometry, a low amount of uniform activity ($\alpha = 0.2\alpha_0$, where α_0 denotes the activity required to nucleate a defect pair) induces the horizontal motion of the +½ defect owing to the asymmetric distribution of active stress[24]. Eventually, this leads to annihilation of the defect pair (Supplementary Video 6). It is therefore of interest to explore how activity gradients could drive motion that deviates from this behaviour. Using the same initial conditions, we selectively activate a rectangular region of

dimensions 290×80 around the +½ defect and consider the effect of rotating the rectangle by an angle ϕ. In Fig. 4a, we show a time sequence of the simulations for $\phi = 45°$ and show that the +½ defect reorients to follow the long axis of the rectangle and deflects its trajectory. This is consistent with the defect deflection observed experimentally (Fig. 1g). Next, we explore how varying the angle ϕ impacts defect trajectories: we find that defects are faithfully guided up to a threshold angle of 60° (Fig. 4b). Above this, defects are no longer reoriented by the patterned activity (Fig. 4c, purple triangles). We then consider how this threshold angle depends on the active stress by systematically varying the activity. Because an activity value greater than α_0 will result in defect creation and not simply redirection, we consider only activities that are less than α_0. When the activity is increased from $0.2\alpha_0$ to $0.3\alpha_0$ and $0.5\alpha_0$, the threshold angle decreases to 45 and 30°, respectively. This can be understood both by the increased defect speed at higher activities and by the effect of activity on the local bend distortion that limits the reorientation of the +½ defect. Thus, as the structured activity approaches α_0, the ability to manipulate individual +½ defects becomes limited. Together with Fig. 3, these data demonstrate how the shape and magnitude of structured activity can be exploited for individual defect generation and manipulation.
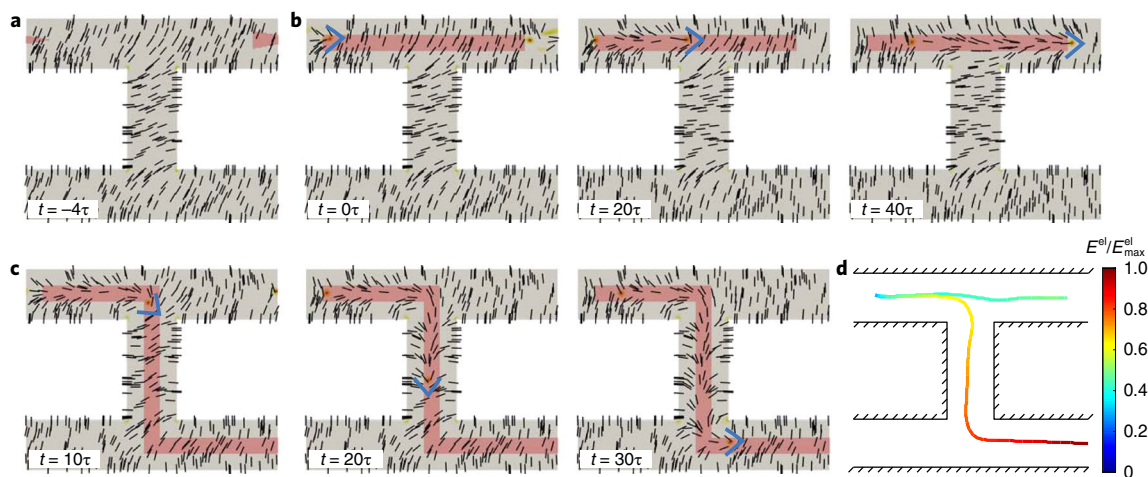
Fig. 6 | Simulations of defect pathway control in a channel system. a, A triangular pattern with activity $\alpha = 1.8\alpha_0$ is used to create a $\pm\frac{1}{2}$ defect pair on an otherwise defect-free channel of width 50 with normal anchoring conditions. Periodic boundary conditions are applied in the x-direction. **b**, Sequential images showing that a $+\frac{1}{2}$ defect moves to the top right channel under a stripe pattern at $\alpha = 0.3\alpha_0$. **c**, Sequential images showing that a $+\frac{1}{2}$ defect moves to the bottom right channel under a 'Z' pattern at $\alpha = 0.4\alpha_0$. The $+\frac{1}{2}$ defect is marked to aid the eye. **d**, Defect trajectories coloured by the system's elastic energy E^{el} for the two types of pattern.

To experimentally test for control over individual defects, we construct quarter-annulus regions in which we stimulate the local activity (Fig. 5a). We performed these experiments under conditions resulting in a low defect density, and no creation of defects upon light stimulus (Supplementary Fig. 1e,f). We start with a $+\frac{1}{2}$ defect at the top left and find that the defect moves and reorients as it follows the pattern (Fig. 5a). This motion results in the defect travelling to the other side of the pattern, rotated 90° from its initial alignment (see Fig. 5a and Supplementary Video 7). This behaviour can be recapitulated both in simulations and in a number of independent samples (Fig. 5b,c). In the case of simulations, one can directly see that the pattern alters the defect's trajectory from what it would be in the case of uniform activity (Supplementary Video 8). Furthermore, the rotation angle probability density function (PDF) of experimental defects in this pattern shows a pronounced, asymmetric peak (Fig. 5d), which indicates that, for the five independent defects considered here, the annulus indeed imposes a preferred turn angle on defects within the region[44]. This is in sharp contrast with a similar histogram constructed from the trajectories obtained from Supplementary Video 1, which shows a relatively uniform, and notably symmetric, distribution at a number of time lags (see Fig. 5e and Supplementary Fig. 9). Note that the stimulation in Supplementary Video 1 occurs over the entire field of view. The observation that the trajectories from the annulus pattern produce a markedly asymmetric angle-change distribution, while a large stimulated region begets a relatively symmetric PDF, provides further evidence that defects are constrained and directed by the pattern. Such defect deflection events, predicted in simulations and observed in experiments, can be understood theoretically by considering the energetic contribution of an activity gradient at the pattern boundary (Supplementary Information and Supplementary Fig. 7).

Control over defects could enable novel devices

To envision how these principles can be applied in microfluidic systems, we demonstrate the control of defect pathways by designing activity patterns in simulations. Specifically, we consider an 'H' channel with two T-junctions containing a defect-free nematic adopting normal anchoring to the surfaces (Fig. 6a–c). We first use a triangular pattern to generate a $\pm\frac{1}{2}$ defect pair (Fig. 6a). Note that if activity is added uniformly through the nematic, the defect will move into the top right channel (Supplementary Fig. 10). To try to exert influence on this fate we consider two different activity patterns: a narrow stripe that is horizontal (Fig. 6b and Supplementary Video 9) or a 'Z' pattern (Fig. 6c and Supplementary Video 9). The $+\frac{1}{2}$ defect is directed along either activity pattern, ultimately being directed into either the top or bottom channel. As these scenarios evolve, the nematic organization is deformed and we can consider how the total elastic energy of the system changes as the defect moves (Fig. 6d). Note that there is a threshold activity below which (for example, $\alpha = 0.3\alpha_0$) the active force is unable to drive the defect to the bottom channel. This observation is consistent with the fact that the total elastic energy of the final state in the case of a stripe pattern is lower than that for the 'Z' pattern. Thus, in simulations, structured activity provides a means to control the defect fate in a microfluidic system, despite distinct trajectories being uphill from an energetic point of view.

Outlook

Spatially structured activity presents a promising direction for engineering structure and transport in an active matter at multiple length scales. For one, defects, and the flows they generate, can be confined on a scale larger than the average defect spacing. This results in steady-state defect-density distributions and promises the types of confined flows seen throughout this work. However, the main promise of this approach is not its ability to merely control bulk flow, but its theoretical specificity at a smaller scale. The number and distribution of defects are key state variables of any nematic system. The ability to specifically nucleate a single defect pair and similarly to be able to manipulate the positions of pre-existing defects are steps along the road to controlling these variables. One could imagine composing these two operations spatially to arbitrarily control the entire nematic director. On a wider scale, the flexibility of spatially structured activity is what excites us the most when thinking of its applications in active systems in general. The ability to exert control in both space and time and across length scales opens the door for programming complex behaviours into active systems. Experimentally, future instances of this system may be tuned by making use of optogenetic motors with varied modulation depths[32,33], or by taking advantage of the dose-dependent responses of populations of motors to select sub-maximal activation levels[33]. One can imagine leveraging such temporal and

spatial control of activity to achieve complex transport tasks or induce novel non-equilibrium steady states. Much work has yet to be done to exert such truly multi-scale control, but we hope that the results presented here may serve as the groundwork for future endeavours.

Online content

Any methods, additional references, Nature Research reporting summaries, source data, extended data, supplementary information, acknowledgements, peer review information; details of author contributions and competing interests; and statements of data and code availability are available at https://doi.org/10.1038/s41563-020-00901-4.

References

1. Ramaswamy, S. The mechanics and statistics of active matter. *Annu. Rev. Condens. Matter Phys.* **1**, 323–345 (2010).
2. Marchetti, M. C. et al. Hydrodynamics of soft active matter. *Rev. Mod. Phys.* **85**, 1143–1189 (2013).
3. Vicsek, T. Novel type of phase transition in a system of self-driven particles. *Phys. Rev. Lett.* **75**, 1226–1229 (1995).
4. Sokolov, A., Mozaffari, A., Zhang, R., de Pablo, J. J. & Snezhko, A. Emergence of radial tree of bend stripes in active nematics. *Phys. Rev. X* **9**, 031014 (2019).
5. Saw, T. B. et al. Topological defects in epthelia govern cell death and extrusion. *Nature* **544**, 212–216 (2017).
6. Kawaguchi, K., Kageyama, R. & Sano, M. Topological defects control collective dynamics in neural progenitor cell cultures. *Nature* **545**, 327–331 (2017).
7. Bricard, A., Caussin, J., Desreumaux, N., Dauchot, O. & Bartolo, D. Emergence of macroscopic directed motion in populations of motile colloids. *Nature* **503**, 95–98 (2013).
8. Kumar, N., Soni, H., Ramaswamy, S. & Sood, A. K. Flocking at a distance in active granular matter. *Nat. Commun.* **5**, 4688 (2014).
9. Dombrowski, C., Cisneros, L., Chatkaew, S., Goldstein, R. E. & Kessler, J. O. Self-concentration and large-scale coherence in bacterial dynamics. *Phys. Rev. Lett.* **93**, 098103 (2004).
10. Li, H. et al. Data-driven quantitative modeling of bacterial active nematics. *Proc. Natl Acad. Sci. USA* **116**, 777–785 (2019).
11. Vizsnyiczai, G. et al. Light controlled 3D micromotors powered by bacteria. *Nat. Commun.* **8**, 15974 (2017).
12. Needleman, D. & Dogic, Z. Active matter at the interface between materials science and cell biology. *Nat. Rev. Mater.* **2**, 17408 (2017).
13. Sanchez, T., Chen, D. T. N., DeCamp, S. J., Heymann, M. & Dogic, Z. Spontaneous motion in hierarchically assembled active matter. *Nature* **491**, 431–434 (2012).
14. Wensink, H. H. et al. Meso-scale turbulence in living fluids. *Proc. Natl Acad. Sci. USA* **109**, 14308–14313 (2012).
15. Giomi, L., Bowick, M. J., Mishra, P., Sknepnek, R. & Marchetti, M. C. Defect dynamics in active nematics. *Phil. Trans. A* **372**, 20130365 (2014).
16. Zhou, S., Sokolov, A., Lavrentovich, O. D. & Aranson, I. S. Living liquid crystals. *Proc. Natl Acad. Sci. USA* **111**, 1265–1270 (2014).
17. Ellis, P. W. et al. Curvature-induced defect unbinding and dynamics in active nematic toroids. *Nat. Phys.* **14**, 85–90 (2018).
18. Keber, F. C. et al. Topology and dynamics of active nematic vesicles. *Science* **345**, 1135–1139 (2014).
19. Guillamat, P., Ignés-Mullol, J. & Sagués, F. Control of active liquid crystals with a magnetic field. *Proc. Natl Acad. Sci. USA* **113**, 5498–5502 (2016).
20. Wu, K. et al. Transition from turbulent to coherent flows in confined three-dimensional active fluids. *Science* **355**, eaal1979 (2017).
21. Opathalage, A. et al. Self-organized dynamics and the transition to turbulence of confined active nematics. *Proc. Natl Acad. Sci. USA* **116**, 4788–4797 (2019).
22. Duclos, G., Yashunsky, V., Salbreux, G., Joanny, J. & Prost, J. Spontaneous shear flow in confined cellular nematics. *Nat. Phys.* **14**, 728–732 (2018).
23. de Gennes, P. G. & Prost, J. *The Physics of Liquid Crystals* (Clarendon Press, 1993).
24. Giomi, L., Bowick, M. J., Ma, X. & Marchetti, M. C. Defect annihilation and proliferation in active nematics. *Phys. Rev. Lett.* **110**, 228101 (2013).
25. Giomi, L. Geometry and topology of turbulence in active nematics. *Phys. Rev. X* **5**, 031003 (2015).
26. Doostmohammadi, A., Ignés-Mullol, J. & Yeomans, J. M. Active nematics. *Nat. Commun.* **9**, 3246 (2018).
27. Kumar, N., Zhang, R., de Pablo, J. J. & Gardel, M. L. Tunable structure and dynamics of active liquid crystals. *Sci. Adv.* **4**, eaat7779 (2018).
28. Thampi, S. P., Golestanian, R. & Yeomans, J. M. Velocity correlations in an active nematic. *Phys. Rev. Lett.* **111**, 118101 (2013).
29. Zhang, R., Kumar, N., Ross, J. L., Gardel, M. L. & de Pablo, J. J. Interplay of structure, elasticity, and dynamics in actin-based nematic materials. *Proc. Natl Acad. Sci. USA* **115**, E124–E133 (2018).
30. Kinosita, K. et al. Dual-view microscopy with a single camera: real-time imaging of molecular orientations and calcium. *J. Cell Biol.* **115**, 67–73 (1991).
31. Sase, I., Miyata, H., Ishiwata, S. & Kinosita, K. Axial rotation of sliding actin filaments revealed by single-fluorophore imaging. *Proc. Natl Acad. Sci. USA* **94**, 5646–5650 (1997).
32. Nakamura, M. et al. Remote control of myosin and kinesin motors using light-activated gearshifting. *Nat. Nanotechnol.* **9**, 693–697 (2014).
33. Ruijgrok, P. V. et al. Optical control of fast and processive engineered myosins in vitro and in living cells. *Nat. Chem. Biol.* (in the press).
34. Ross, T. D. et al. Controlling organization and forces in active matter through optically defined boundaries. *Nature* **572**, 224–229 (2019).
35. Linsmeier, I. et al. Disordered actomyosin networks are sufficient to produce cooperative and telescopic contractility. *Nat. Commun.* **7**, 12615 (2016).
36. Schindler, T. D., Chen, L., Lebel, P., Nakamura, M. & Bryant, Z. Engineering myosins for long-range transport on actin filaments. *Nat. Nanotechnol.* **9**, 33–38 (2014).
37. Beris, A. N. & Edwards, B. J. *Thermodynamics of Flowing Systems: with Internal Microstructure* (Oxford Univ. Press, 1994).
38. Marenduzzo, D., Orlandini, E., Cates, M. & Yeomans, J. Steady-state hydrodynamic instabilities of active liquid crystals: hybrid lattice Boltzmann simulations. *Phys. Rev. E* **76**, 031921 (2007).
39. Aditi Simha, R. & Ramaswamy, S. Hydrodynamic fluctuations and instabilities in ordered suspensions of self-propelled particles. *Phys. Rev. Lett.* **89**, 058101 (2002).
40. Zhang, R., Zhou, Y., Rahimi, M. & de Pablo, J. J. Dynamic structure of active nematic shells. *Nat. Commun.* **8**, 13483 (2016).
41. Shankar, S. & Marchetti, M. C. Hydrodynamics of active defects: from order to chaos to defect ordering. *Phys. Rev. X* **9**, 041047 (2019).
42. Shen, M., Li, H. & Olvera de la Cruz, M. Surface polarization effects on ion-containing emulsions. *Phys. Rev. Lett.* **119**, 138002 (2017).
43. Thampi, S. P., Golestanian, R. & Yeomans, J. M. Instabilities and topological defects in active nematics. *Europhys. Lett.* **105**, 18001 (2014).
44. Burov, S. et al. Distribution of directional change as a signature of complex dynamics. *Proc. Natl Acad. Sci. USA* **110**, 19689–19694 (2013).

Methods

Protein purification. Monomeric actin was purified from rabbit skeletal muscle acetone powder (Pel-Freez Biologicals) as described previously[45] and stored in G-buffer (2 mM Tris buffer pH 8, 0.2 mM ATP, 0.5 mM dithiothreitol, 0.1 mM CaCl$_2$, 1 mM NaN$_3$, pH to 8). Actin was labelled with tetramethylrhodamine-6-maleimide (TMR; Life Technologies). F-actin Capping Protein (CP) was a gift from the laboratory of D. Kovar and was purified according to the method in ref. [46].

The optically gear-shifting engineered tetrameric myosin motors were the based on the myosin XI construct MyLOVChar4~1R~TET described in ref. [33], and a variant with the same lever-arm structure but with mutations to an actin-binding loop in the catalytic domain of myosin XI (MyLOVChar4$_{L2(+4)}$~1R~TET). The mutations introduce four positive charges to actin-binding loop 2, denoted as the mutation L2(+4) in ref. [47], modifying the wild-type loop sequence FPADEGT**K**APS**K**FMSIG into FPADEG*GGKKGG*T**K**APS**KKK**FMSIG (with positive charges in bold, altered amino acids in italic). These mutations to loop 2 have been reported to result in an eightfold increase of apparent actin binding affinity in actin-activated ATPase assays, and a fourfold decrease of velocity in gliding motility assays[47]. The myosin proteins were purified as described[33], flash frozen in small aliquots and stored at −80 °C. Upon removal from the −80 °C freezer, aliquots were used immediately as described below. The myosin constructs include a HaloTag and were labelled with the Alexa 660 fluorophore during purification (Halotag Alexa Fluor 660 Ligand, Promega).

Assay conditions. Actin filaments were polymerized at a concentration of 2 µM in 50 µl of various assay buffers. All experiments contained oxygen-scavenging reagents [2.7 mg ml^{-1} glucose oxidase (catalogue no. 345486, Calbiochem), 1700 U ml^{-1} catalase (catalogue no. 02071, Sigma), 4.5 mg ml^{-1} glucose, 0.5% v/v β-mercaptoethanol, prepared at 50× in 1x F-buffer and 2% glycerol] and 0.3% w/v methylcellulose (viscosity 15 cP) as a crowding agent. Experiments were buffered with either F-buffer (10 mM imidazole, 1 mM MgCl$_2$, 50 mM KCl, 0.2 mM egtazic acid, pH 7.5) (Fig. 1) or F-buffer-HEPES (10 mM HEPES, 1 mM MgCl$_2$, 50 mM KCl, 0.2 mM egtazic acid, 1 mM imidazole, pH 7.5) (Fig. 5) with ~100 µm ATP, in the presence of ~20 nM CP. The actin mixture that was polymerized contained a 1:5 ratio of TMR-labelled to unlabelled monomers. To ensure that the polymerization was complete, mixtures were incubated on ice for one hour before imaging. For a summary of assay conditions for specific experiments see Supplementary Table 1.

The imaging chamber was created by first rinsing a small glass cloning cylinder (catalogue no. 09-552-20, Corning) with ethanol and then attaching it to an activated coverslip with two-part epoxy resin. To prevent the actin from sticking and to maintain fluidity the coverslip was first coated with a thin layer of Novec 7500 Engineered Fluid (3M) that included PFPE-PEG-PFPE surfactant (catalogue no. 008, RAN Biotechnologies) at 2% w/v to stabilize the oil–water interface. To coat the chamber, ~4 µl of the oil and surfactant mixture was pipetted into the bottom of the chamber and then quickly removed. To minimize evaporation, the polymerized actin and methylcellulose mixture was quickly added to the coated chamber. After addition, the actin mixture was allowed to sit for 20 min so that the actin was given time to crowd onto the oil–water interface and form the liquid crystal. Gear-shifting motors MyLOVChar4~1R~TET (Fig. 1) were first diluted into F-buffer and then pipetted directly into the sample chamber. MyLOVChar4$_{L2(+4)}$~1R~TET motors (Fig. 5) were diluted fivefold into 1x F-buffer-HEPES and 5% v/v glycerol. Two microlitres of this dilution was pipetted into the sample chamber. For a full summary of motor additions see Supplementary Table 1.

The sample was imaged using an Eclipse-Ti inverted microscope (Nikon) in confocal mode utilizing a spinning disk (CSU-X; Yokogawa Electric) and a CMOS camera (Zyla-4.2 USB 3; Andor). The experiment in Fig. 1 was imaged using a ×60, 1.20 numerical aperture multi-immersion objective (Nikon) whereas the data in Fig. 5 were collected using a ×40, 1.15 numerical aperture water immersion objective (Nikon). The TMR fluorophore was excited using a 561 nm continuous wave fibre laser (VFL-P series; MPB Communications) at a rate of one frame every four seconds (for ×60 experiments) or one frame every five seconds (for ×40 objective experiments). Microscope components were controlled via the software package MetaMorph (Molecular Devices). Activation was achieved by illuminating the sample with a 400 mW, 470 nm light-emitting diode (ThorLabs) targeted to the region outlined in red in Figs. 1 and 5 (Supplementary Videos 2 and 6, respectively) using a mosaic micromirror array (Andor). During the period of activation the sample was exposed to the activation wavelength continuously for two seconds of the four-second frame rate or for three seconds of the five-second frame rate.

Image and data analysis. Velocity fields were calculated using the method of optical flow detailed in ref. [48] using the Matlab code available at (https://ps.is.mpg.de/code/secrets-of-optical-flow-code-for-various-methods) and the 'classic+nl-fast' method. Velocity plots were generated using Matlab. The defect density and defect trajectories were plotted using the Matplotlib library in Python. The PDF of the relative angle change given a time lag was calculated using the method detailed in ref. [44] with a modified definition of the angle. To summarize,

we first construct the vector $V(t,\Delta) = X(t+\Delta) - X(t)$ from the trajectory of a defect given by $X(t)$. The angle between adjacent vectors is calculated as

$$\theta = \sin^{-1}\left(\frac{(V(t,\Delta) \times V(t+\Delta,\Delta)) \cdot \hat{z}}{|V(t)||V(t+1)|}\right) \quad (1)$$

where $(V(t,\Delta) \times V(t+\Delta,\Delta)) \cdot \hat{z}$ denotes the magnitude of the cross product, $|V(t)|$ denotes the Euclidean norm, and $\sin^{-1}$ denotes the inverse sine function. The probability density of θ is shown in Fig. 5c,d with $n = 15$ bins evenly spaced between −90 and 90°.

The velocity correlation length quoted in Supplementary Fig. 2 is calculated as

$$\xi = \int dr \frac{v_i(0), v_j(r)}{|v_i||v_j|} \quad (2)$$

where i,j denotes the inner product.

Defect localization and tracking. In two dimensions, the core of a defect is a point where we cannot define the local director field, which is the average orientation of all filaments in that region and is denoted by the unit vector $\hat{n}$. The charge of a defect is given by $\frac{1}{2\pi}\oint d\phi$, where ϕ is the angle between $\hat{n}$ and a reference vector. The intensity of any given pixel in the image is given by $I_i = I_o + \cos^2(\phi_i - \omega)$, where ω is the angle of the polarization of the laser, ϕ_i is the angle of the local director field and I_o accounts for the fact that orthogonal directions do not truly exhibit zero intensity. The cosine squared function induces a symmetry such that two angles at the same distance from the polarization axis (that is, $\theta \pm \varepsilon$) exhibit the same intensity. Because of this polarization symmetry, assigning a director field to every pixel algorithmically is difficult. Thus, in this work we focus instead on the position of defects, which can be readily identified because they are surrounded by all angles of the director field and thus both the highest and lowest pixel intensities in the frame. Defects in these movies have a characteristic shape and look like triangular wedges of either bright (dark) pixels extending into a patch of dark (bright) pixels. We can assign charge by considering the wedge. If the intensity of the wedge indicates that the filaments in this region are aligned along (against) the axis of the wedge, the defect in question carries a charge of +½ (−½). Defects are tracked manually using the manual tracking plugin in ImageJ (https://imagej.nih.gov/ij/plugins/track/track.html, 2005 version).

Simulation model. *Theoretical model.* The bulk free energy of the nematic liquid crystal, F, is defined as

$$F = \int_V dV f_{bulk} + \int_{\partial V} dV f_{surf} = \int_V dV(f_{LdG} + f_{el}) + \int_{\partial V} dV f_{surf}, \quad (3)$$

where the bulk free energy density f_{bulk} is comprised of f_{LdG}, the short-range free energy, and f_{el}, the long-range elastic energy. f_{surf} is the surface free energy due to anchoring. The parameter f_{LdG} is given by a Landau–de Gennes expression of the form[23,49]:

$$f_{LdG} = \frac{A_0}{2}\left(1 - \frac{U}{3}\right)\text{Tr}(\mathbf{Q}^2) - \frac{A_0 U}{3}\text{Tr}(\mathbf{Q}^3) + \frac{A_0 U}{4}\text{Tr}(\mathbf{Q}^2)^2. \quad (4)$$

Parameter U controls the magnitude of q_0, namely the equilibrium scalar order parameter via $q_0 = \frac{1}{4} + \frac{1}{4}\sqrt{1 - \frac{8}{3U}}$. The elastic energy f_{el} under one-constant approximation is written as ($Q_{ij,k}$, which means $\partial_k Q_{ij}$):

$$f_{el} = \frac{1}{2}L_1 Q_{ij,k}Q_{ij,k}. \quad (5)$$

Point wise, $\mathbf{n}$ is the eigenvector associated with the greatest eigenvalue of the Q-tensor at each lattice point.

To simulate the liquid crystal's non-equilibrium dynamics, a hybrid lattice Boltzmann method is used to simultaneously solve a Beris–Edwards equation and a momentum equation which accounts for the hydrodynamic effects. By introducing a velocity gradient $W_{ij} = \partial_k u_i$, strain rate $A = (W + W^T)/2$, vorticity $\Omega = (W − W^T)/2$, and a generalized advection term

$$S(\mathbf{W},\mathbf{Q}) = (\xi\mathbf{A} + \mathbf{\Omega})(\mathbf{Q} + \mathbf{I}/3) + (\mathbf{Q} + \mathbf{I}/3)(\xi\mathbf{A} - \mathbf{\Omega}) \\ - 2\xi\left(\mathbf{Q} + \frac{\mathbf{I}}{3}\right)\text{Tr}(\mathbf{QW}), \quad (6)$$

one can write the Beris–Edwards equation[37] according to

$$(\partial_t + \mathbf{u} \cdot \nabla)\mathbf{Q} - S(\mathbf{W},\mathbf{Q}) = \Gamma\mathbf{H}. \quad (7)$$

The constant ξ is related to the material's aspect ratio, and Γ is related to the rotational viscosity γ_1 of the system[50] by $\Gamma = 2q_0^2/\gamma_1$. The molecular field $\mathbf{H}$, which drives the system towards thermodynamic equilibrium, is given by

$$\mathbf{H} = -\left[\frac{\delta F}{\delta\mathbf{Q}}\right]^{st}, \quad (8)$$

where $[\ldots]^{st}$ is a symmetric and traceless operator. When velocity is absent, that is $u(r) \equiv 0$, the Beris–Edwards equation reduces to the Ginzburg–Landau equation:

$$\partial_t\mathbf{Q} = \Gamma\mathbf{H}. \quad (9)$$

Using an Einstein summation rule, the momentum equation for the nematics can be written as[37,51]

$$\rho(\partial_t + u_j \partial_j) u_i = \partial_j \Pi_{ij} + \eta \partial_j \left[\partial_i u_j + \partial_j u_i + (1 - 3\partial_\rho P_0) \partial_k u_k \delta_{ij} \right] - \gamma u_i, \tag{10}$$

where η is the isotropic viscosity and γ is the frictional coefficient. The stress $\Pi_{ij} = \Pi_{ij}^{\mathrm{p}} + \Pi_{ij}^{\mathrm{a}}$ consists of a passive and an active part. The passive stress Π_{ij}^{p} is defined as

$$\Pi_{ij}^{\mathrm{p}} = -P_0 \delta_{ij} - \xi H_{ik} \left(Q_{kj} + \tfrac{1}{3}\delta_{kj} \right) - \xi \left(Q_{ik} + \tfrac{1}{3}\delta_{ik} \right) H_{kj} \\ + 2\xi \left(Q_{ij} + \tfrac{1}{3}\delta_{ij} \right) Q_{kl} H_{kl} - \partial_j Q_{kl} \tfrac{\delta F}{\delta \partial_i Q_{kl}} \\ + Q_{ik} H_{kj} - H_{ik} Q_{kj}, \tag{11}$$

in which the hydrostatic pressure P_0 is given by

$$P_0 = \rho T - f_{\mathrm{bulk}}. \tag{12}$$

The temperature T is related to the speed of sound c_s by $T = c_s^2$. The active stress reads[38]

$$\Pi_{ij}^{\mathrm{a}} = -\alpha Q_{ij}, \tag{13}$$

in which α is the activity in the simulation. The stress is extensile when $\alpha > 0$ and contractile when $\alpha < 0$.

Numerical details. We solve the Beris–Edwards equation using a finite-difference method. The momentum equation is solved simultaneously via a lattice Boltzmann method over a D3Q15 grid[52]. The implementation of stress follows the approach proposed by Guo et al.[53]. The units are chosen as follows: the unit length a is chosen to be $a = \xi_N = 1\,\mu m$, comparable to the filament length; the characteristic viscosity is set to $\gamma_1 = 0.1\,\mathrm{Pa\,s}$; and the force scale is made to be $F_0 = 10^{-11}\,\mathrm{N}$. These choices give rise to a unit stress being $10\,\mathrm{N\,m^{-1}}$. Other parameters are chosen to be $A_0 = 0.1$, $L_1 = 0.1$, $\xi = 0.8$, $\Gamma = 0.13$, $\eta = 1.0$, $\gamma = 0.01$ and $U = 3.5$, leading to $q_0 \cong 0.62$. The simulation is performed on a square lattice with a periodic boundary condition. Simulation results are expressed in terms of a time unit τ, which maps onto 2.6 s in our experimental system. Flow and direction in the third dimension are enforced to be zero to enforce a two-dimensional condition. Defect localization is implemented by identifying low scalar order parameter grid points (with $q < 0.45$), which are grouped into defects according to their spatial connectivity. The topological charge or the winding number of individual defects is obtained by numerically calculating the loop integral over the surrounding points. Tracking is performed manually, as in experiments. We refer the reader to ref. [4] for additional details on the numerical methods employed here.

Data availability
All experimental image data are available on the Dryad server (https://doi.org/10.5061/dryad.7wm37pvr6). Additional data are available upon request.

Code availability
The custom analysis script used to make the histograms in Fig. 5 and Supplementary Fig. 9 is available at github.com/Gardel-lab.

References
45. Spudich, J. A. & Watt, S. The regulation of rabbit skeletal muscle contraction. I. Biochemical studies of the interaction of the tropomyosin-troponin complex with actin and the proteolytic fragments of myosin. *J. Biol. Chem.* **246**, 4866–4871 (1971).
46. Palmgren, S., Ojala, P. J., Wear, M. A., Cooper, J. A. & Lappalainen, P. Interactions with PIP$_2$, ADP-actin monomers, and capping protein regulate the activity and localization of yeast twinfilin. *J. Cell Biol.* **155**, 251–260 (2001).
47. Ito, K., Yamaguchi, Y., Yanase, K., Ichikawa, Y. & Yamamoto, K. Unique charge distribution in surface loops confers high velocity on the fast motor protein *Chara* myosin. *Proc. Natl Acad. Sci. USA* **106**, 21585–21590 (2009).
48. Sun, D., Roth, S. & Black, M. J. Secrets of optical flow estimation and their principles. In *Proc. IEEE Conf. on Computer Vision and Pattern Recognition* 2432–2439 (IEEE, 2010).
49. Landau, L. D. & Lifshitz, I. M. *Statistical Physics* (Butterworth-Heinemann, 1980).
50. Denniston, C., Orlandini, E. & Yeomans, J. M. Lattice Boltzmann simulations of liquid crystal hydrodynamics. *Phys. Rev. E* **63**, 056702 (2001).
51. Denniston, C., Marenduzzo, D., Orlandini, E. & Yeomans, J. M. Lattice Boltzmann algorithm for three-dimensional liquid-crystal hydrodynamics. *Phil. Trans. A* **362**, 1745–1754 (2004).
52. Guo, Z. & Shu, C. *Lattice Boltzmann Method and Its Applications in Engineering* (World Scientific Publishing Company, 2013).
53. Guo, Z., Zheng, C. & Shi, B. Discrete lattice effects on the forcing term in the lattice Boltzmann method. *Phys. Rev. E* **65**, 046308 (2002).

Acknowledgements

Author contributions
R.Z., S.A.R., N.K., M.L.G. and J.J.d.P. conceived the research. R.Z. performed simulations with help from A.M.; S.A.R. performed experiments. P.V.R., S.Z. and Z.B. contributed novel reagents and expertise. R.Z. and S.A.R. performed data analysis. N.K., A.M., V.V. and A.R.D. contributed to analysis and interpretation. M.L.G. and J.J.d.P. supervised the research. R.Z., S.A.R., M.L.G. and J.J.d.P. wrote the manuscript. Everyone contributed to the discussion and manuscript revision.

Competing interests

Additional information